IEEE Access
Multidisciplinary | Rapid Review | Open Access Journal

Received 30 January 2025, accepted 13 February 2025, date of publication 19 February 2025, date of current version 25 February 2025.

Digital Object Identifier 10.1109/ACCESS.2025.3543659

RESEARCH ARTICLE

Adaptive Sliding Mode Control of a Boost Converter With Unknown Constant Power Load

DAVID A. ZAMBRANO-PRADA[1], ABDELALI EL AROUDI[1], (Senior Member, IEEE), OSWALDO LÓPEZ-SANTOS[1], (Senior Member, IEEE), LUIS VÁZQUEZ-SEISDEDOS[2], AND LUIS MARTÍ-NEZ-SALAMERO[1], (Life Senior Member, IEEE)

[1]Group of Automatic Control and Industrial Electronics (GAEI), Department of Electrical, Electronic and Automatic Control Engineering, School of Electrical and Computer Engineering, Rovira i Virgili University, Campus Sescelades, 43007 Tarragona, Spain
[2]Department of Forestry Engineering and Management, School of Forestry Engineering and Natural Resources, Electrotechnics Teaching Unit, Technical University of Madrid, 28040 Madrid, Spain

Corresponding author: David A. Zambrano-Prada (davidalejandro.zambrano@urv.cat)

This work was supported by the Ministerio de Ciencia, Innovación y Universidades (MICIU)/Agencia Estatal de Investigación (AEI)/10.13039/501100011033/Fondo Europeo de Desarrollo Regional (FEDER), Union Europea (UE), under Project PID2023-150839OB-I00.

ABSTRACT In this paper, output voltage regulation in a boost converter with constant power load (CPL) is carried out by means of sliding-mode control (SMC) with an estimation loop of the output power. The estimation procedure is based on the integral of an odd-symmetric function of the output voltage error, which confers an adaptive nature to the switching regulator. Rational, trigonometric, sigmoid and sign-type odd-symmetric functions are analyzed to select the best candidate for output power estimation. In addition, a two-degree polynomial surface is considered to induce the sliding motions. Subsequently, the corresponding conditions for the existence of the sliding mode and for the stability of the equilibrium point including the estimation dynamics are derived. One of the main features of this proposal is that the resulting controller can be implemented analogically, requiring operational amplifier-based circuits plus a divider. PSIM© and MATLAB© simulations show a fast recovery in response to large-signal disturbances in the load power and zero steady-state output voltage error. Experimental results obtained from a 500 W prototype are in perfect agreement with both theoretical predictions and numerical simulations.

INDEX TERMS Constant power load, boost converter, adaptive power estimation, sliding-mode control.

I. INTRODUCTION

Constant power load (CPL) is currently a usual operation mode in the multi-converter systems of different energy processing applications such as powertrains in electric vehicles (EVs) [1], power supplies for telecommunications [2], and microgrids for decentralized electricity generation [3]. The canonical description of a multi-converter system in CPL operation is a dc-to-dc switching converter loaded with a nonlinear one-port device, whose current (i) - voltage (v) characteristic is the hyperbola described by:

$$i(t)v(t) = P, \quad i, v, P \in R^{+} \tag{1}$$

where P is the constant power absorbed by the device. The symbol of a CPL is a power sink as shown in Fig. 1a, where the current absorbed by the device is expressed as P/v. Fig. 1b, in turn, depicts the corresponding $i-v$ characteristic.

Converters supplying a CPL in open-loop and discontinuous conduction mode (DCM) are stable but become unstable when operating in continuous conduction mode (CCM) [4]. Therefore, they require in CCM an appropriate closed-loop strategy to stabilize them and regulate their output voltage. They may also need the insertion in some cases of additional damping networks to reinforce the stabilization.

Linear controllers that cope with the instability of power converters under CPL condition are based on an unstable control to output transfer function which is derived by simple substitution of the resistive load of a conventional case by the negative incremental resistance of the CPL. The steady-state values of the state variables required in the transfer function are the ones imposed by the closed-loop operation assuming that an appropriate controller has stabilized the system [5].

The associate editor coordinating the review of this manuscript and approving it for publication was Zhe Zhang.

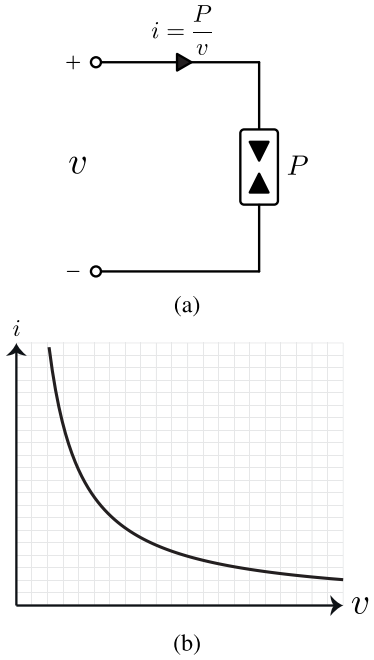

FIGURE 1. Instantaneous constant power load (a) Symbol (b) Current-voltage characteristics.

In addition, passive damping can be used to stabilize the cascade connection of a voltage source, an LC filter and a CPL without altering the source or the load control [6]. On the other hand, active damping is based on the emulation of a virtual resistance by an appropriate control, which is obtained by feedback linearization in [7] or current control [8], [9], or by the synthesis of a loss-free resistor (LFR) that is inserted in series with the input port of the converter to compensate the negative incremental resistance of the CPL [10].

Nonlinear controllers are of boundary type as in the work reported in [11] or of sliding-mode control (SMC) nature [12]. The latter approach is applied in [13] and verified by simulation in the output voltage regulation of a boost converter that supplies the parallel connection of a CPL and a resistive load using a switching function which is a linear combination of the capacitor voltage error and the difference between the inductor current and its high-frequency component. SMC is also used in a PWM implementation in [14] at constant switching frequency using a nonlinear switching surface which is slightly modified in [15] to improve the output voltage regulation in a prototype operating at variable switching frequency. Switching surfaces based on current error or on linear combinations of current and voltage errors are used in a SMC-based PWM implementation to regulate the dc bus of a dc microgrid with photovoltaic panels, a battery bank and several boost converters [16]. Moreover, the use of SMC in combination with an output current observer has been proven by simulation to be a reliable solution to control a dual active bridge with constant power load [17].

The combination of the unstable trajectories of the boost converter with a CPL during ON and OFF states by means of an appropriate switching policy has resulted in [18] in a stable trajectory with an excellent performance in the output voltage regulation without using an integral action in the controller. The latter approach has been generalized in [19] by the introduction of polynomial surfaces and a systematic analysis of the optimal selection of the sliding surface minimizing the inrush current while keeping an accurate voltage regulation. SMC has also been proved to be an effective tool in a cascaded control strategy of the quadratic buck converter interfacing a domestic 380 V dc bus to a CPL requiring a regulated voltage of 48 V [20].

Most of the works devoted to the control of power converters with CPL use the nominal value of the constant power P in the analysis of the system and therefore in the synthesis of the controller. The design of the latter involves a complex off-line mathematical analysis to determine the optimal values of the controller parameters, which are not modified during the converter operation. The performance of the controller is determined in terms of robustness, which indicates the variation degree of the regulated variable for large deviations of the actual output power from the nominal value P [21]. Another example of this approach is the work reported in [22], in which a power shaping control is used to regulate the output voltage of buck, boost and buck-boost converters feeding a load made up of the parallel connection of CPL, resistor, and current source with unknown parameters.

In a clear-cut contrast, adaptive controllers estimate the value of the CPL power online to modify the controller parameters accordingly. They are based on an uncertain value of P, which is included in the control strategy as illustrated in the output voltage regulation of a buck-boost analyzed in [23] and modified in [24] by means of a change of coordinates and partial linearization. The latter technique is used in a buck converter [25], which also has been analyzed for CPL power estimation [26], [27], [28] in combination with high-order sliding-mode observers [29], [30]. The boost converter with unknown CPL has also been the subject of different studies. In this sense, the energy shaping control approach described in [23] and [24] is applied to a boost converter with CPL in [31]. Moreover, the insertion of a nonlinear disturbance observer gives adaptive behavior to a passivity-based control in [32] and feedforward compensation for output voltage regulation in [33]. The mentioned works regarding adaptive controllers are characterized by a rigorous continuous-time theoretical analysis and by a complex digital implementation in which the absence of a previous discretization analysis makes the experiments interpretation difficult.

Regarding implementation of the resulting controllers, both digital and analog has been reported. SMC with adaptive characteristics and digital implementation has been used successfully for power factor correction in a full wave rectifier supplying a boost converter operating as a LFR [34] and in a semi-bridgeless boost converter using an estimation loop of the reference current profile based on O-splines [35]. On the other hand, the main reference of analog

implementation of nonlinear controllers for output voltage regulation of a power converter with CPL using an estimation loop of the CPL power has been reported in [36], in which the analysis is based on a continuous–time model and the estimation is performed by the integral of a nonlinear function with odd-symmetry of the output voltage error.

With the aim of regulation of the output voltage through an analog implementation, this paper introduces the continuous-time analysis of a CPL boost converter using SMC with an estimation loop of the CPL power that processes the integral of the function an-odd symmetric of the output voltage error. The work reported here is an extension of a preliminary version presented in [37], in which it was verified by simulation that both a parabolic switching function of the inductor current and a hyperbolic switching function of the product of inductor current and capacitor voltage with a power estimation given by the integral of the output voltage error allowed the output voltage regulation for unknown values of the CPL power. It was shown in that paper that the parabolic switching function exhibited the best performance. The extension presented here is based on the general polynomial surface proposed in [19], whose terms depending of the inductor current are modified by the difference between the inductor current and the ratio of the estimated CPL power and input voltage. The other estimated variable is the integral of an output error function whose main analytical characteristics are initially defined and whose subsequent realization is studied in several possible cases.

More specifically, the main contributions of this paper are:

- A systematic method is established for the design of sliding-mode controllers based on polynomial surfaces that incorporate the output power estimation in the analytical expression of the switching described by the sliding surface.
- The power estimation is achieved from the integration of an odd function of the error between the output voltage and its desired reference. The strategy allows not only to estimate the CPL power value, but also to guarantee a zero output voltage error. The paper discusses the necessary and sufficient conditions that the odd function must satisfy, and analyzes the estimation potentiality of four families of functions.
- Sliding-mode and local stability conditions of the closed-loop system with the power estimator are established. The small-signal results are qualitatively extrapolated to provide insight of the system's large-signal operation.
- A first-order sliding-mode controller and a linear power estimator are both implemented using analog electronics. In comparison with other proposals, the implementation is simpler in terms of circuitry and results in larger power range and better response to a step power variation in the CPL.

The rest of the paper is organized as follows. A general polynomial switching surface with power estimation by means of voltage error function for SMC of the boost converter with a CPL is described in Section II. The conditions for existence and stability of sliding motions are analyzed in Section III. Section IV defines the properties of the voltage error functions used for power estimation loop and four types of candidate functions are presented. The main features of the resulting adaptive behavior are discussed in Section V. Simulation and experimental results are illustrated in Section VI. The conclusions of the paper are summarized in the last Section.

II. SLIDING MODE CONTROLLER WITH POWER ESTIMATION

A. POWER CONVERTER DESCRIPTION

Fig. 2 shows the circuit diagram of a boost converter supplying a CPL, whose voltage-current characteristic is given by $i_{CPL} = P/v_C$, where P is the power of the CPL and v_C is the output capacitor voltage. The voltage-current characteristic is represented in Fig. 2. The complementary diode D_r in Fig. 2 is added to pre-charge the output capacitor and to improve the start-up of the converter by establishing the initial voltage $v_C(0) = V_g$.

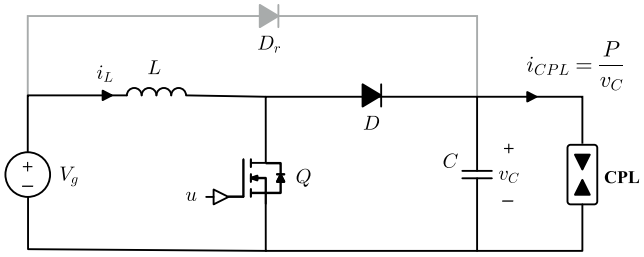

FIGURE 2. Schematic circuit diagram of a boost converter with CPL and a complementary diode D_r.

The system equations describing the boost converter with CPL in CCM can be expressed as follows

$$L\frac{di_L}{dt} = V_g - (1-u)v_C \tag{2a}$$

$$C\frac{dv_C}{dt} = i_L(1-u) - \frac{P}{v_C} \tag{2b}$$

where i_L is the non-negative inductor current, V_g is the input voltage and u is a binary driving signal, so that $u = 1$ for on state and $u = 0$ for off state. C and L are the capacitance of the output capacitor and the inductance of the inductor, respectively.

B. TWO-DEGREE POLYNOMIAL SWITCHING SURFACE

The general polynomial switching surface analyzed in [19] is modified by introducing a variable that represents the estimation $\hat{P}$ of the output power P, as can be seen in (3). Note that switching function (3) corresponds to a family of conic curves in the $i_L - v_C$ phase plane, that are centered in

the origin in the particular case of an ellipse.

$$\begin{aligned} S_p(x) = a_2\left(i_L^2 - \frac{\widehat{P}^2}{V_g^2}\right) + b_2\left(v_C^2 - V_e^2\right) \\ + 2\left(hi_L v_C - \frac{\widehat{P}V_e}{V_g}\right) \\ + 2a_1\left(i_L - \frac{\widehat{P}}{V_g}\right) + 2b_1\left(v_C - V_e\right) \\ \times a_1, a_2, b_1, b_2, h \in R^+ \end{aligned} \tag{3}$$

In expression (3), V_e is the desired output voltage while the relation $\widehat{P}/V_g$ sets an adaptive current reference reflecting the POPI nature of the boost converter [38]. This means that the dc output power equals the dc input power in steady state when $\hat{P} \triangleq P$, which implies that the equilibrium point (EP) of the system X_e is given by $X_e = [P/V_g, V_e]^\intercal$.

C. A GENERAL DESCRIPTION OF THE POWER ESTIMATOR

The dynamic behavior of the estimated power variable $\hat{P}$ can be defined as a function of the voltage error $e_v(t) = v_C - V_e$ as it was demonstrated in [36] and [37] for a nonlinear and a linear function, respectively. In an attempt to generalize, we define now a power estimation function as follows

$$\frac{d\hat{P}}{dt} = f(e_v) \tag{4}$$

In steady-state, one has

$$\hat{P} = \int_{-\infty}^{t} f(e_v)d\tau \approx \int_{0}^{T_s} f(e_v)d\tau = P \tag{5}$$

where $f(0) = 0$ at the finite time T_s. Thus, the integral of the function $f(e_v)$ provides the estimation of the CPL and ensures the regulation of the output voltage with zero steady-state error. Also, the power estimation function must satisfy the conditions given in (6) in order to guarantee the convergence of the system to EP.

$$f(e_v)\, e_v < 0 \tag{6a}$$

$$f(-e_v) = -f(e_v) \tag{6b}$$

$$\frac{df(e_v)}{de_v}\Big|_{X_e} = -\beta, \quad \beta > 0 \tag{6c}$$

III. CONDITIONS OF EXISTENCE AND STABILITY OF SLIDING MOTION

A. CONDITIONS OF EXISTENCE OF SLIDING MOTION

Let $x = [i_L,\ v_C]^\intercal$ and $\Sigma = \{x|\ S_p(x) = 0\}$, sliding motions on the switching surfaces Σ will exist if the condition $\dot{S}_p(x)S_p(x) < 0$ is satisfied [12]. From (3), $\dot{S}_p(x)$ is given by

$$\begin{aligned} \dot{S}_p(x) = \frac{\left(V_g - v_C(1-u)\right)\left(a_2 i_L + hv_C + a_1\right)}{L} \\ + \frac{\left(i_L(1-u) - P/v_C\right)\left(b_2 v_C + hi_L + b_1\right)}{C} \\ - \frac{f(e_v)}{V_g}\left(\frac{a_2\hat{P}}{V_g} + hV_e + a_1\right) \end{aligned} \tag{7}$$

The above expression is rewritten in (8) to express explicitly the incremental resistance $r(x)$ defined in [19].

$$\begin{aligned} \dot{S}_p(x) = \left(\frac{CV_g r(x)}{L} + \frac{P}{v_C} + \frac{C\hat{r}(x)f(e_v)}{V_g}\right) \\ - \left(\frac{Cv_C r(x)}{L} + i_L\right)(1-u) \end{aligned} \tag{8}$$

where the incremental resistance $r(x)$ is given by

$$r(x) = -\frac{a_2 i_L + hv_C + a_1}{b_2 v_C + hi_L + b_1} \tag{9}$$

and its estimated value $\hat{r}(x)$ can be expressed as

$$\hat{r}(x) = -\frac{\frac{a_2\hat{P}}{V_g} + hV_e + a_1}{b_2 v_C + hi_L + b_1} \tag{10}$$

Thus, there is a region of existence of sliding motions (ESM) if the following conditions are satisfied.

$$\lim_{S_p \to 0^+} \dot{S}_p = \frac{P}{v_C} - i_L - \frac{Cr(x)(v_C - V_g)}{L} + \frac{C\hat{r}(x)f(e_v)}{V_g} < 0 \tag{11a}$$

$$\lim_{S_p \to 0^-} \dot{S}_p = \frac{CV_g r(x)}{L} + \frac{P}{v_C} + \frac{C\hat{r}(x)f(e_v)}{V_g} > 0 \tag{11b}$$

Then, combining expressions (11a) and (11b) in a single inequality leads to the following ESM region

$$i_L < \frac{P}{v_C} - \frac{Cr(x)(v_C - V_g)}{L} + \frac{C\hat{r}(x)f(e_v)}{V_g} \tag{12}$$

Within the ESM region and after reaching the switching surface, the sliding dynamics along Σ guarantee the fulfillment of the invariance conditions $S_p(x) = 0$ and $\dot{S}_p(x) = 0$. As a result, the ideal sliding dynamics of the system can be described in terms of an average model, which is based on the equivalent control u_{eq}, the latter being bounded between 0 and 1, i.e. $0 \le u_{eq} \le 1$ according to (12).

$$u_{eq} = 1 - \frac{\frac{Cr(x)V_g}{L} + \frac{P}{v_C} + \frac{C\hat{r}(x)f(e_v)}{V_g}}{i_L + \frac{Cv_C r(x)}{L}} \tag{13}$$

Introducing the equivalent control (13) in (2), the ideal sliding dynamics is obtained and shown at the bottom of the next page in (14a)-(14c). To simplify the equations corresponding to the expression (14c), we define $N(i_L, v_C, \hat{P}) \triangleq \frac{CV_g r(x)}{L}\left(i_L - \frac{P}{V_g}\right) + \frac{C\hat{r}(x)f(e_v)}{V_g}$ and $D(i_L, v_C, \hat{P}) \triangleq i_L + \frac{Cv_C r(x)}{L}$.

It is worth to note that the system dynamics given in (14) is nonlinear and its core is the set of state variables v_C and $\hat{P}$ given by equations $y_1(x)$ and $y_2(x)$, which corresponds to a second order system. On the other hand, i_L is a function of v_C and $\hat{P}$ and its partial derivatives with respect to these state variables are given by the expressions (15a) and (15b).

$$\frac{\partial i_L}{\partial v_C}\Big|_{X_e} = \frac{1}{r(x)}\Big|_{X_e} = -\frac{\frac{a_2 P}{V_g} + hV_e + a_1}{b_2 V_e + \frac{hP}{V_g} + b_1} = -\frac{1}{R} \tag{15a}$$

$$\frac{\partial i_L}{\partial \hat{P}}\Big|_{X_e} = \frac{1}{V_g} \tag{15b}$$

B. STABILITY ASSESSMENT

In order to determine the stability conditions, the ideal sliding dynamics of the system given by equations (14a)-(14c) is linearized around the EP to obtain its small-signal dynamics. This approach provides the local stability of the system. At EP, the incremental resistance and its estimated value are equal, i.e., $r(x)|_{X_e} = \hat{r}(x)|_{X_e} = -R$. The linearization of y_2 is based on equation (6c) and only depends on v_C. On the other hand, since $N(i_L, v_C, \hat{P}) = 0$ at EP, the linearization of y_1 requires the calculation of expression (16), where $z = [v_C, P]^\intercal$.

$$\frac{\partial y_1}{\partial z_j} = \left.\frac{\left(\frac{\partial N}{\partial z_j} + \frac{\partial N}{\partial i_L}\frac{\partial i_L}{\partial z_j} + \frac{\partial N}{\partial r}\frac{\partial r}{\partial z_j} + \frac{\partial N}{\partial \hat{r}}\frac{\partial \hat{r}}{\partial z_j}\right)}{D}\right|_{X_e} \tag{16}$$

It is worth to note that for the sake of simplifying the notation, $N(i_L, v_C, \hat{P})$ and $D(i_L, v_C, \hat{P})$ have been written as N and D in (16). Also when developing (16), it can be observed that the terms concerning the partial derivatives of $r(x)$ and $\hat{r}(x)$ are cancelled at EP because of the values $I_L^* = P/V_g$ and $V_C^* - V_e = 0$. Hence, the small-signal dynamics can be described by

$$\frac{d\tilde{v}_C}{dt} = -\frac{\left(\frac{V_g}{L} - \frac{RP\beta}{V_g^2}\right)\tilde{v}_C - \frac{R}{L}\tilde{p}}{\frac{CV_eR}{L} - \frac{P}{V_g}} = -\frac{B\tilde{v}_C - \Gamma\tilde{p}}{\Lambda} \tag{17a}$$

$$\frac{d\tilde{p}}{dt} = -\beta\tilde{v}_C \tag{17b}$$

where $\Lambda = \frac{CV_eR}{L} - \frac{P}{V_g}$, $B = \frac{V_g}{L} - \frac{RP\beta}{V_g^2}$, and $\Gamma = \frac{R}{L}$.

Therefore, the Jacobian matrix corresponding to (17) can be expressed as follows

$$J = \begin{bmatrix} \left.\frac{\partial y_1}{\partial v_C}\right|_{X_e} & \left.\frac{\partial y_2}{\partial \hat{P}}\right|_{X_e} \\ \left.\frac{\partial y_1}{\partial v_C}\right|_{X_e} & \left.\frac{\partial y_2}{\partial \hat{P}}\right|_{X_e} \end{bmatrix} = \begin{bmatrix} -\frac{B}{\Lambda} & \frac{\Gamma}{\Lambda} \\ -\beta & 0 \end{bmatrix} \tag{18}$$

and the characteristic equation corresponding to the previous Jacobian matrix is given by

$$\det(s\mathbb{I} - J) = \begin{vmatrix} s + \frac{B}{\Lambda} & -\frac{\Gamma}{\Lambda} \\ \beta & s \end{vmatrix} = s^2 + \frac{B}{\Lambda}s + \frac{\Gamma\beta}{\Lambda} \tag{19}$$

From (19), the joint operation of sliding-mode controller with power estimation will be stable if all coefficients of the characteristic equation are positive. By simple inspection, the following necessary conditions for stability are derived. For $\Lambda > 0$ the upper limit of output power load is defined

$$P < \frac{RCV_eV_g}{L} \triangleq P_{max} \tag{20}$$

and for $B > 0$, the upper limit of the parameter β is given by

$$\beta < \frac{V_g^3}{LPR} \triangleq \beta_{max} \tag{21}$$

It has to be pointed out that the upper output power limit does not depend on the value of the linear estimator gain. Furthermore, the maximum allowable gain of the estimation loop is independent of the type of switching surface. This limit is only associated to the converter input and output power and the values of inductance and incremental resistance at EP. Therefore, any switching surface fulfilling the previous conditions will result in the same limit. In addition, the convergence of the power estimator is directly connected to the stability of the system. If the latter is ensured for small variations around X_e, the linearized system will have asymptotical stability, and exponential convergence in the power estimator will be guaranteed.

Table 1 presents a particularization of expression (3) in steady-state for five polynomial switching surfaces corresponding to canonical curves; namely, affine curve (one-degree curve), current parabola, voltage parabola, cross-power hyperbola and ellipse (two-degree curves).

It is worth noting that $S_{p2c}(x)$ corresponds to the hyperbolic switching surface studied in [37], but the parabolic current switching surface in that work is different from S_{p2a}. The coefficients of the parabola in [37] are time-varying and modify the parabola shape during transients. In contrast, the set of switching surfaces defined in (3) uses constant coefficients and keeps the curve shape unchanged during transients.

Complementary, Fig. 3 shows the five polynomial switching surfaces in the phase plane $i_L - v_C$ using the values of Table 2 for an absolute value of the incremental resistance of $R = 20\ \Omega$ at EP where $I_L = P/V_g$. The value of R

$$i_L = -\frac{hv_C + a_1}{a_2} + \sqrt{\left(\frac{hv_C + a_1}{a_2} + \frac{\hat{P}^2}{V_g^2}\right)^2 - \frac{(v_C - V_e)\left(b_2\left(v_C + V_e\right) + 2b_1\right)}{a_2}} \tag{14a}$$

$$\frac{dv_C}{dt} = \frac{\frac{CV_gr(x)}{L}\left(i_L - \frac{P}{V_g}\right) + \frac{C\hat{r}(x)f(e_v)}{V_g}}{i_L + \frac{Cv_Cr(x)}{L}} \triangleq y_1(x) \tag{14b}$$

$$\frac{d\hat{P}}{dt} = f(e_v) \triangleq y_2(x) \tag{14c}$$

TABLE 1. Particular cases of polynomial switching surfaces with power estimation loop.

Polynomial curves	Coefficients in (3)	Surface
Affine	$a_2 = b_2 = h = 0$	$S_{p1}(x) = a_1\left(i_L - \frac{\hat{P}}{V_g}\right) + b_1(v_C - V_e)$
Current parabola	$a_1 = b_2 = h = 0$	$S_{p2a}(x) = a_2\left(i_L^2 - \frac{\hat{P}^2}{V_g^2}\right) + 2b_1(v_C - V_e)$
Voltage parabola	$a_2 = b_1 = h = 0$	$S_{p2b}(x) = b_2\left(v_C^2 - V_e^2\right) + 2a_1\left(i_L - \frac{\hat{P}}{V_g}\right)$
Cross-power Hyperbola	$a_2 = a_1 = 0$ $b_2 = b_1 = 0$	$S_{p2c}(x) = h\left(i_L v_C - \frac{\hat{P}V_e}{V_g}\right)$
Ellipse	$a_2 = b_2 = h = 0$	$S_{p2d}(x) = a_2\left(i_L^2 - \frac{\hat{P}^2}{V_g^2}\right) + b_2\left(v_C^2 - V_e^2\right)$

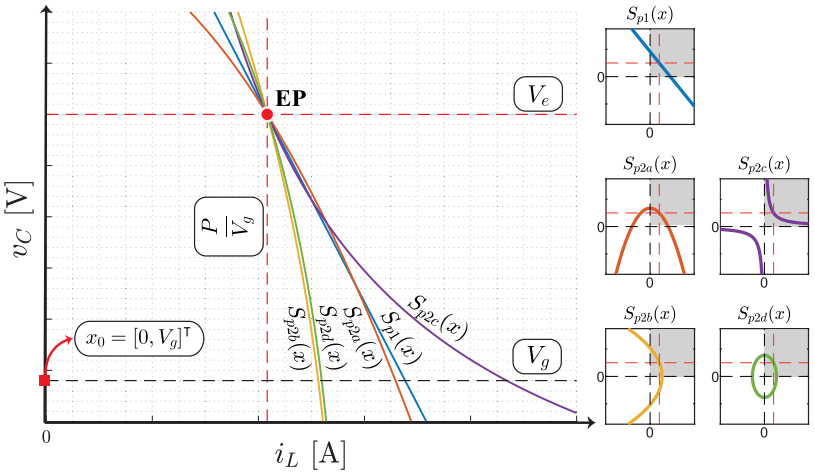

FIGURE 3. Phase-plane $i_L - v_C$ for five polynomial surfaces in steady-state with an absolute value of the incremental resistance $R = 20\ \Omega$ for $P = 240$ W, $V_g = 48$ V, and $V_e = 100$ V.

was chosen considering the surface $S_{p2c}(x)$, which depends only on X_e. The figure is divided into two parts: the right side shows a magnification of each surface centered at the origin. Instead, the left side depicts a zoomed view around EP. The intersection between the surface and the horizontal axis $v_C = V_g$ determines the maximum peak of i_L when starting from $x_0 = [0, V_g]^\intercal$ due to the complementary diode D_r in Fig. 2. With the exception of the hyperbolic curve, the conic surfaces provide a lower value of inrush current than the affine surface in start-up [19].

IV. CANDIDATE FUNCTIONS FOR POWER ESTIMATION

The conditions for the power estimator outlined in (4) and (6) represent functions with odd symmetry. These functions will be used as in classical linear control by integrating the error, the linear expression $-\beta e_v$ being the simplest example of them [37].

Another example is reported in [36], where a nonlinear voltage error function is used for power estimation in a PWM nonlinear control. However, that work has been selected the estimator with no systematic approach.

TABLE 2. Surface coefficient for $R = 20\ \Omega$ used in Fig. 3.

Surface	a_2	b_2	h	a_1	b_1
$S_{p1}(x)$	0	0	0	2	0.1
$S_{p2a}(x)$	1	0	0	0	0.25
$S_{p2b}(x)$	0	0.001	0	4	0
$S_{p2c}(x)$	0	0	4	0	0
$S_{p2d}(x)$	0.8	0.001	0	0	0

In the next subsections, four types of candidate functions that satisfy the requirements for power estimation are presented.

A. RATIONAL FUNCTIONS

Expression (22) illustrates a general rational function for a power estimation loop. To fulfil the specified requirements, the degree of the numerator must be odd and that of the

denominator even.

$$f_1(e_v) = -\frac{\beta {e_v}^{2m-1}}{1+\alpha {e_v}^{2n}} \tag{22}$$

The coefficients m and n are positive integers. The linear estimator in [37] is a special case of (22) when $m = 1$ and $\alpha = 0$ (23a), and the nonlinear estimator presented in [36] results from choosing $m = 1$ and $n = 1$ (23b).

$$f_{1a}(e_v) = -\beta e_v \tag{23a}$$

$$f_{1b}(e_v) = -\frac{\beta e_v}{1+\alpha {e_v}^2} \tag{23b}$$

The derivative of f_1 with respect to e_v is given by:

$$\frac{\partial f_1}{\partial e_v} = -\frac{\beta}{1+\alpha {e_v}^{2n}}\left((2m-1)\,{e_v}^{2m-2} - 2n\alpha {e_v}^{2m+2n-2}\right) \tag{24}$$

By inspection at $e_v = 0$, it can be concluded that m equal to 1 is the only appropriate value of m to guarantee that $\partial f_1(e_v)/\partial e_v$ is $-\beta$. For $m > 1$ the function exhibits odd symmetry, the estimated power $\hat{P}$ tends to the actual power P, but at $e_v = 0$ the partial derivative $\partial f_1(e_v)/\partial e_v$ is zero. On the other hand, there is no constraint on the parameter n, so $n \in \mathbb{N}$ with a correct selection of parameter α.

An advantage of the rational function when $n \neq 0$ and the degree of the numerator is lower than that of the denominator is the possibility to limit the maximum estimated power value; otherwise, the estimator function will be unbounded. Therefore, there exists a value $\|f_1\|_\infty = P_{max}$, which takes place at points $e_v = \pm e_{v_o}$ given by

$$e_{v_o} = \sqrt[2n]{\frac{2m-1}{2n\alpha}} \tag{25}$$

By introducing (25) in (22), we obtain

$$|f(e_{v_o})| = \left|\frac{\beta\left(\frac{2m-1}{2n\alpha}\right)^{\frac{2m-1}{2n}}}{1+\frac{2m-1}{2n}}\right| \tag{26}$$

Fig. 4 represents three rational functions described by equations (23a), (23b) and (27) for the range -100 V$< e_v <$100 V, $\beta = 10$ kA/s and the parameters of Table 3, in which f_{max} is the maximum value of the function in the range. Note that f_{1a} is the simplest and the only unbounded function of the group.

$$f_{1c}(e_v) = -\frac{\beta e_v}{1+\alpha {e_v}^4} \tag{27}$$

B. TRIGONOMETRIC FUNCTIONS

There are two functions that use trigonometric expressions and satisfy the power estimator conditions, i.e. sine and tangent functions with the following equations:

$$f_{2a}(e_v) = -\frac{\beta \sin(\alpha e_v)}{\alpha} \tag{28a}$$

$$f_{2b}(e_v) = \frac{\beta \tan(\alpha e_v)}{\alpha} \tag{28b}$$

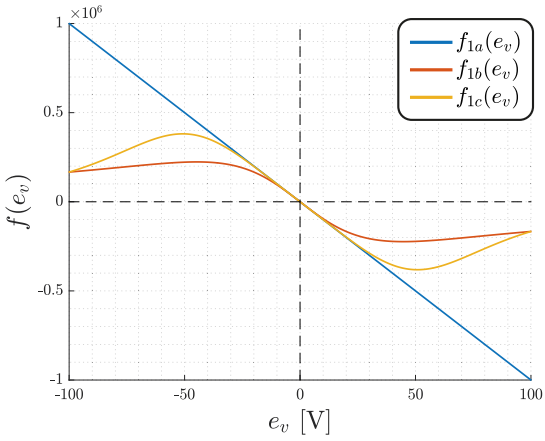

FIGURE 4. Rational functions corresponding to (23a), (23b) and (27).

TABLE 3. Rational functions' parameters.

Function	α	f_{max}
f_{1a}	0	1000 kW/s
f_{1b}	0.05	223.6 kW/s
f_{1c}	0.05	381.1 kW/s

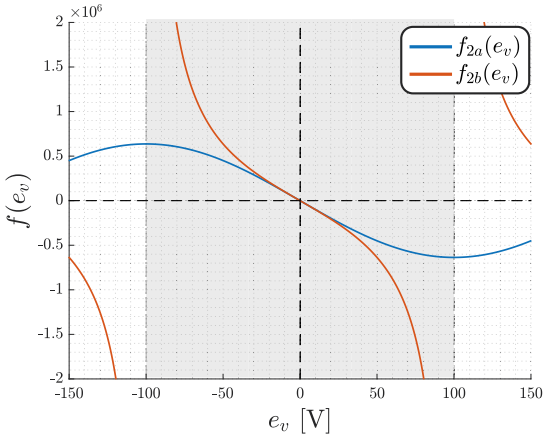

FIGURE 5. Trigonometric functions corresponding to (28a) and (28b).

To ensure a one-to-one correspondence and therefore a single equilibrium point, the domain of both functions is limited to the range $-\pi/2 < \alpha e_v < \pi/2$, with a value of $\alpha = \pi/200$, which implies $|\alpha e_v| = \pi/2$ for a maximum value of $|e_v| = 100$ V. The shaded region in Fig. 5 represents the range of operation of the functions in (28) for $\beta = 10$ kA/s. Note that the tangent function within this region tends to $\pm\infty$ near to the maximum value of $|e_v|$, what makes this solution unfeasible for large excursions of the error.

C. SIGMOID FUNCTIONS

Sigmoids are functions that present a monotonic S-shape characteristic. Conditions in (6) restrict sigmoid functions

TABLE 4. Rational functions' parameters.

Function	$\frac{\partial f}{\partial e_v}$	$\lvert f_{max}\rvert$	α
f_{3a}	$-\frac{\beta \exp^{\alpha e_v}}{(1+\alpha \exp^{\alpha e_v})^2}$	$\frac{2\beta}{\alpha}$	0.1
f_{3b}	$-\frac{\beta}{1+\alpha^2 {e_v}^2}$	$\frac{\pi\beta}{2\alpha}$	0.06
f_{3c}	$-\beta \text{sech}^2(\alpha e_v)$	$\frac{\beta}{\alpha}$	0.05
f_{3d}	$-\frac{\beta}{(1+\alpha {e_v}^2)^{3/2}}$	$\frac{\beta}{\sqrt{\alpha}}$	0.002

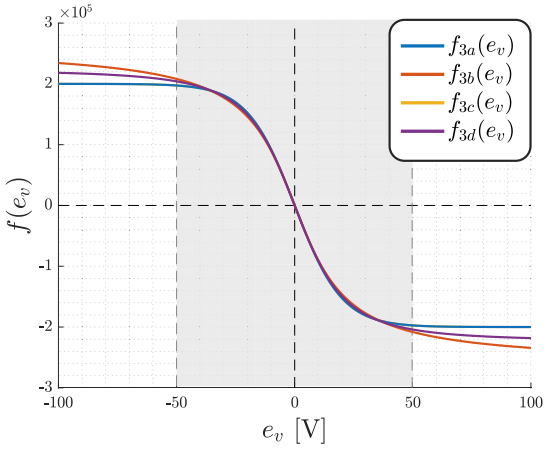

FIGURE 6. Sigmoid functions corresponding to functions in Table 4.

to be monotonic decreasing. There are several equations that can represent them. Expressions (29) list four of the most commonly used sigmoid functions and Table 4 shows their derivatives, maximum value and associated parameter. It can be observed that all of them exhibit $\partial f_3/\partial e_v = -\beta$ at $e_v = 0$.

$$f_{3a(e_v)} = -\frac{2\beta}{\alpha}\left(1 - \frac{2}{1+\exp^{\alpha e_v}}\right) \tag{29a}$$

$$f_{3b}(e_v) = -\frac{\beta \arctan(\alpha e_v)}{\alpha} \tag{29b}$$

$$f_{3c}(e_v) = -\frac{\beta \tanh(\alpha e_v)}{\alpha} \tag{29c}$$

$$f_{3d}(e_v) = -\frac{\beta e_v}{\sqrt{1+\alpha {e_v}^2}} \tag{29d}$$

Fig. 6 depicts the four sigmoid functions for a value of β =10 kA/s and illustrates a well-known feature of sigmoid functions, i.e., the existence of two horizontal asymptotes that limit the function with symmetrical constant values when the error approaches theoretically $\pm\infty$. Note that (i) the functions are very similar in the four cases differing slightly in the maximum value, and that (ii) f_{3a} and f_{3c} can be made equal for an appropriate choice of α.

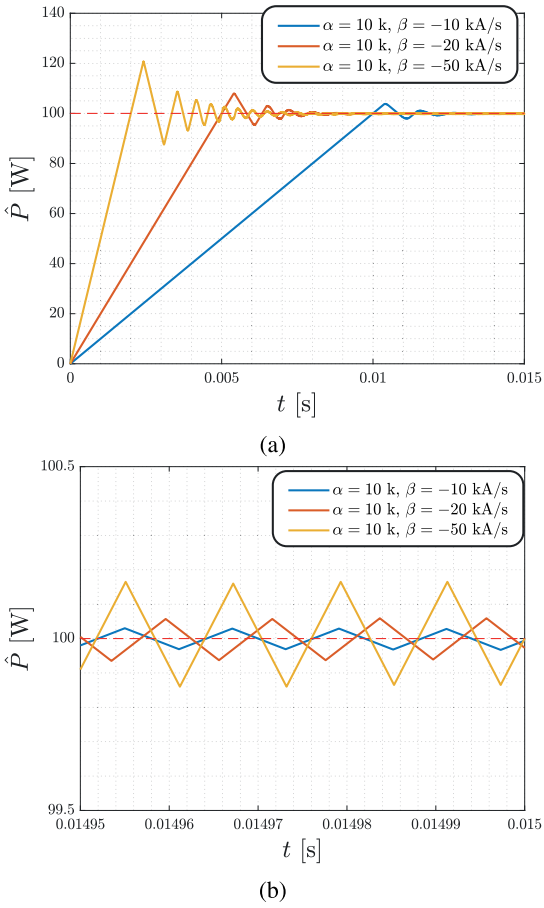

FIGURE 7. Estimated output power by a first-order sliding-mode estimator. (a) From start-up to steady-state regime. (b) Zoom in steady-state showing the switching of the sliding estimator.

D. FIRST-ORDER SLIDING ESTIMATOR

A special case results when considering the sign function defined in (30) as a candidate function for a power estimator:

$$f_{4a}(e_v) = -\beta \,\text{sign}(\alpha e_v) \begin{cases} \alpha e_v < 0 & f_{4_a} = \beta \\ \alpha e_v = 0 & f_{4_a} = 0 \\ \alpha e_v > 0 & f_{4_a} = -\beta \end{cases} \tag{30}$$

Strictly speaking, the sing function would not fulfill the condition (6c), because its derivative at the origin is not defined. However, similarly to the unbounded rational functions with $m > 1$, the closed-loop dynamics using the estimator with f_{4a} will tend to EP but without remaining there. As illustrated in Fig. 7, the estimated output power will be confined in a permanent sliding motion around EP, provided that the system disturbances cannot move the closed-loop dynamics away from the EP neighborhood.

This fact can be understood as the typical feature of an ideal sliding estimator, where the average value of the estimation corresponds to the value of the load power. The ideal sliding estimator operates at infinite switching frequency, which is impractical for implementation. A bounded approximation

reported in [13] and described in (31), produces a finite frequency and also fulfills the abovementioned conditions for power estimation

$$f_{4b}(e_v) = \begin{cases} -\beta \operatorname{sign}(\alpha e_v) & \alpha e_v \geq \varepsilon \\ -\beta \alpha e_v & \alpha e_v < \varepsilon \end{cases} \tag{31}$$

The parameter ε is the bandwidth of the approximation and determines the switching frequency of the power estimation $\hat{P}$. On the other hand, parameter β must fulfill the inequality $P < \beta < \beta_{max}$ to ensure the reachability and invariance conditions on the sliding surface.

V. CHARACTERISTICS OF THE ADAPTIVE SLIDING CONTROLLER WITH POWER ESTIMATION

A. SMALL-SIGNAL DYNAMICS

The dynamic behavior associated to the polynomial surfaces analyzed in sections II and III can be represented in sliding mode around EP by the following second-order linear homogeneous differential equation, which represents the ideal sliding dynamics

$$\frac{d^2\tilde{v_C}}{dt^2} + \frac{B}{\Lambda}\frac{d\tilde{v_C}}{dt} + \frac{\beta\Gamma}{\Lambda}\tilde{v_C} = 0 \tag{32}$$

where the superscript $(\sim)$ stands for small variations of v_C around its equilibrium value. By considering the effect of the external variation of the power reference (ΔP) and output voltage reference (ΔV_e), and applying the Laplace transform, the system dynamics can be represented by means of the block diagram in Fig. 8.

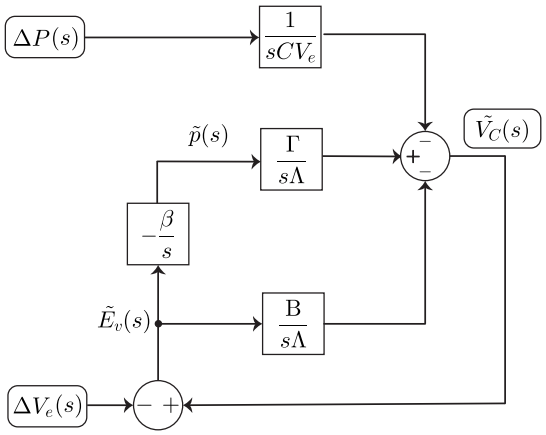

FIGURE 8. Block diagram of the small-signal dynamics of the boost converter in sliding motion including output power and voltage reference variations.

By examining the coefficients of the characteristic equation in (32), it can be concluded that the incremental resistance $|r(x)|_{X_e} = R$ mainly determines the sliding dynamics as demonstrated in [19]. This means that for small-signal variations, the same dynamic behavior will be obtained in all sliding-mode controllers using a polynomial surface with the same values of R and power estimation gain β irrespective of the specific estimation function employed.

TABLE 5. Converter and reference values.

Parameter	Value
L	115 μH
C	50 μF
P	240 W
V_g	48 V
V_e	100 V

In order to prove the accuracy of the model depicted in Fig. 8 for small-signal disturbances, Fig. 9 and Fig. 10 show the response of the system to a power load variation from 240 W to 200 W and to a voltage reference change from 100 V to 105 V, respectively. The confirmation has been performed by comparing the analytical predictions with simulations in PSIM© using an incremental resistance at EP $R = 4\ \Omega$, a power estimation gain $\beta = 10$ kA/s, and the parameters in Table 5. In both responses, the simulation is in perfect agreement with the theoretical prediction.

After the verification of the analytical model in the vicinity of EP, different values of power estimation gain β with fixed value of $R = 4\ \Omega$ have been tested under an abrupt change of load power as illustrated in Fig. 11. A high-gain value generates a better rejection of disturbances but produces an underdamped behavior in the power estimation. Nevertheless, there is no big difference in the settling time for all the values of β due to the combined effect of the sliding motion and the power estimator.

In addition, Fig. 12 shows the response of the system for different values of incremental resistance R and a fixed value of $\beta = 10$ kA/s. A high value of R makes the underdamping behavior worse. We can define an upper limit of R given by $R_{max} \triangleq V_e V_g / P = 20\ \Omega$, which corresponds to the intrinsic incremental resistance value of $S_{p2c}(x)$, so that higher values of R can lead to oscillating behavior. On the other hand, the lower limit for R is derived from (20) and is equal to

$$R_{min} \triangleq \frac{LP}{CV_e V_g} \tag{33}$$

B. APPROXIMATE INSIGHT INTO LARGE-SIGNAL DYNAMICS

The analysis and simulation of the linearized model show certain key aspects of sliding mode control with power estimation that can provide a qualitative description in a large-signal analysis. The main conclusion is that the sliding dynamics can be described in terms of its incremental resistance $\partial v_C / \partial i_L$ at EP. However, other aspects regarding the exact boundaries of stability are still open. For instance, the stability conditions imposed in terms of both maximum value of the power load and power estimation loop gain are

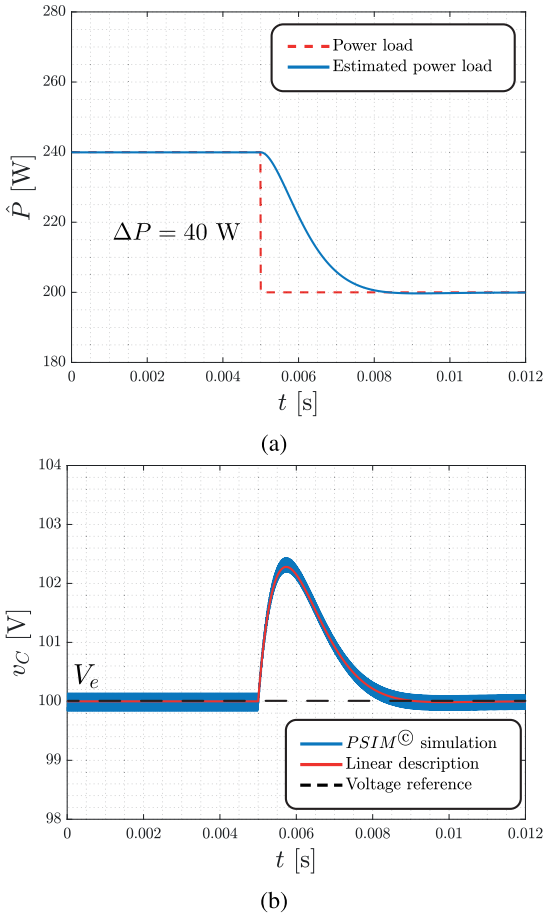

FIGURE 9. Small-signal comparison between analytical and PSIM© simulation responses to a power load disturbance. (a) Power estimation response. (b) Output voltage rejection.

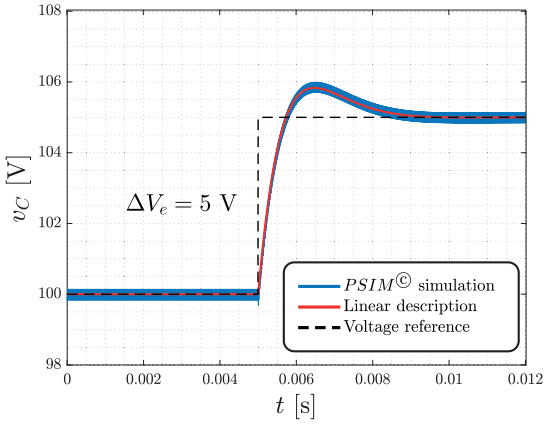

FIGURE 10. Comparison of analytical and PSIM© simulation responses to a voltage reference variation.

conservative due to simplifying approximations, and they depend on some of the system parameters.

In order to give an approximate insight into the large-signal dynamics, a complementary approach is to study the evolution of the system during start-up from the initial condition $x_o = [0,\ V_g,\ 0]^\intercal$ up to the EP defined by

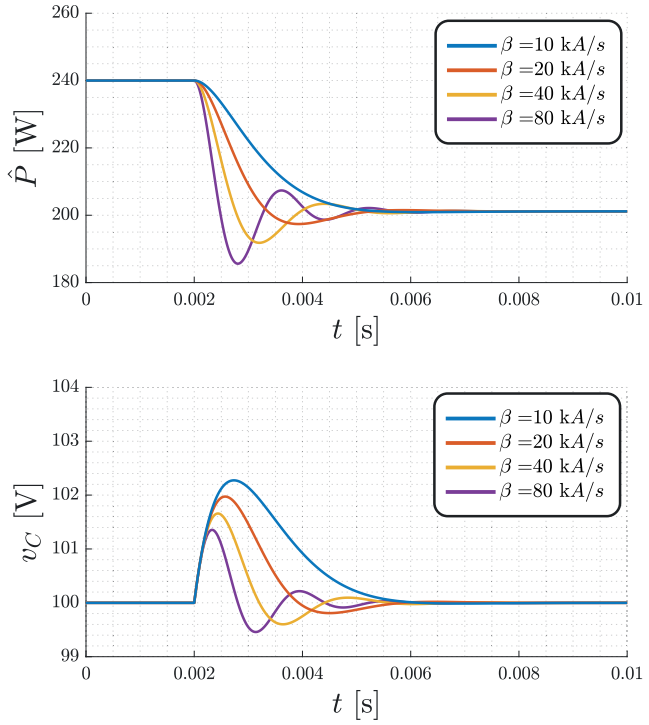

FIGURE 11. Small-signal response to an abrupt change of load power from 240 W to 200 W for four values of estimator gain and the same incremental resistance $R = 4\ \Omega$.

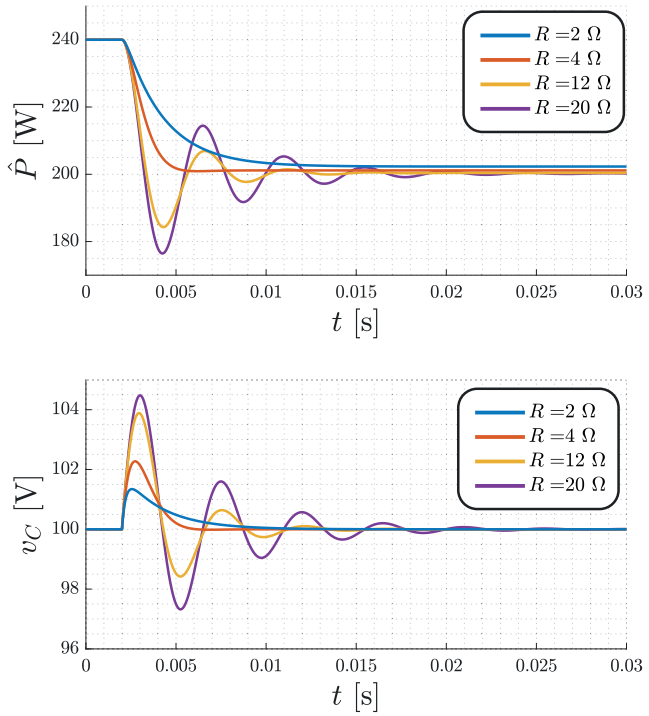

FIGURE 12. Small-signal response to an abrupt change of load power from 240 W to 200 W for four values of incremental resistance R and β =10 kA/s.

$X_e = [P/V_g,\ V_e,\ P]^\intercal$ using simulations in PSIM© and MATLAB©, and the parameter values given by Table 5.

TABLE 6. Surface coefficient for $R = 4\ \Omega$.

Surface	a_2	b_2	h	a_1	b_1
$S_{p1}(x)$	0	0	0	0.4	0.1
$S_{p2a}(x)$	1	0	0	0	1.25
$S_{p2b}(x)$	0	0.001	0	0.4	0
$S_{p2d}(x)$	0.8	0.001	0	0	0

Fig. 13 shows the state variables of the five polynomial surfaces studied with $\beta = 10$ kA/s and the coefficients given by Table 2, they corresponding to $R = 20\ \Omega$ (upper limit of R defined in the previous section). For all cases, the estimator convergence is achieved with an underdamped behavior and similar settling time, where the best performance corresponding to the surface $S_{p2c}(x)$; it should be noted that this surface does not provide any degree of freedom in the controller design so the upper limit in R is automatically imposed by the surface itself. For the other surfaces, the higher the degree of the polynomial is, the higher the overshoot in the state variables results, the affine curve having the lowest overshoot.

Complementary, Fig. 14 illustrates the evolution of the incremental resistance along the trajectory for each polynomial surface, which is calculated by means of expression (9). As the power estimation loop is associated to the current reference, in the surfaces where algebraic powers with the corresponding coefficients are dominant, e.g., $S_{p2a}(x)$ and $S_{p2d}(x)$, the behavior of the system in closed-loop is more underdamped due to the interaction between both control and estimation loops.

Nonetheless, by choosing a value of $R = 4\ \Omega$ with the coefficients given by Table 6, according to Section V-A, a critical damping performance of the closed-loop system is obtained even in the large-signal situation of the start-up as illustrated in Fig. 15. Note that with this design constraint, the hyperbolic surface is excluded. It can be observed that the behavior of the output voltage is similar for all surfaces exhibiting close settling time values. As shown in Fig. 15, canonical surfaces have a lower inrush current because the system reaches the surface and the estimator converges faster [19]. On the one hand, the current peak decreases as the degree of the polynomial increases as illustrated in the same figure. In addition, this feature is compensated by the slightly underdamped performance of the power estimation, whose oscillating behavior scarcely increases when the degree of the polynomial increases.

Analyzing further the information in Figs. 14-16 to understand the influence of the control parameters is the natural sequel of the small-signal study described above. In this sense, Fig. 16 illustrates the roots location of the closed-loop equation (32) when $r(x)$ varies from 1 Ω to 100 Ω and the values of β and P are constant. The shadowed area

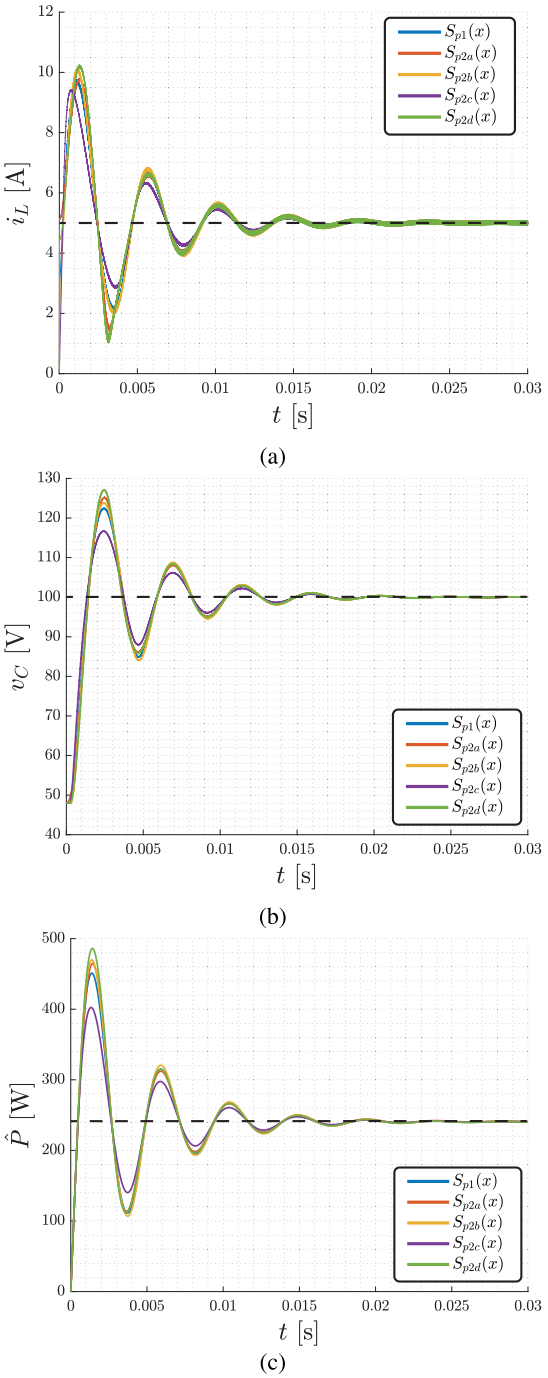

FIGURE 13. PSIM© simulation of state variables during start-up for polynomial surfaces with $R = 20\ \Omega$. (a) i_L. (b) v_C. (c) $\widehat{P}$.

corresponds to the region where the roots of the closed-loop system have a damping factor equal to or greater than 0.4. Note that the responses depicted in Figs. 15-16 can be justified now by the location of the corresponding closed-loop poles in the complex plane of Fig. 17. Similarly, the almost identical responses with critical damping of all surfaces in Fig. 15 for $R = 4\ \Omega$ can be explained by the location of the poles in the mentioned region.

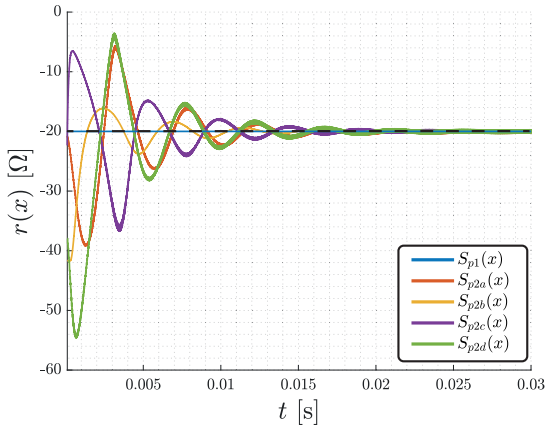

FIGURE 14. Incremental resistance $r(x)$ vs time along the trajectory from x_0 at $R = 20$ Ω.

Fig. 18 and Fig. 19 show the closed-loop pole location for variations of the power estimation gain β and output power load respectively, and $R = 4$ Ω. It can be concluded from Fig. 19 that the pole location is practically unaffected by the large variations of the load power.

Comparing the surfaces in terms of implementation complexity and taking into account that the small-signal description and the resulting large-signal behavior are defined mainly by the incremental resistance, it can be concluded that the sliding mode controller with affine surface is the best practical option because it ensures a fixed $r(x)$ value along the entire state-vector trajectory for large-signal operations such as start-up or large variation of load power. This feature guarantees the achievement of the design theoretical predictions in a wide range of practical operating values of the boost converter supplying a CPL with an unknown value of power P.

C. EFFECT OF CONDUCTION LOSSES AT EP

The proposed power estimation loop calculates the power supplied by the input source through the relation $i_L = P/V_g$. In steady-state and absence of losses, the estimated power corresponds to the output power, but in the presence of power losses (conduction and switching losses) the estimated power corresponds to the power of the load plus the power losses in the converter itself. In the latter case, the power estimation error at EP is defined as $E_p = P - \hat{P}$ and is given by

$$E_p = \frac{V_g}{2R_{Loss}}\left(V_g - \sqrt{V_g^2 - 4PR_{Loss}}\right) - P \qquad (34)$$

where R_{Loss} summarizes the effect of the parasitic resistances in the converter and is the main source of losses. The expression (34) is the result of the power balance in the converter and is therefore independent of the control method. Thus, the error of power estimation is a function of parasitic resistance and output load power. In practice, with a highly efficient converter, it is common to find R_{Loss} values less than 1 Ω. In the case of a 500 W load and $R_{Loss} = 0.1$ Ω, this would represent a maximum deviation of 12 W (i.e. 97% of efficiency).

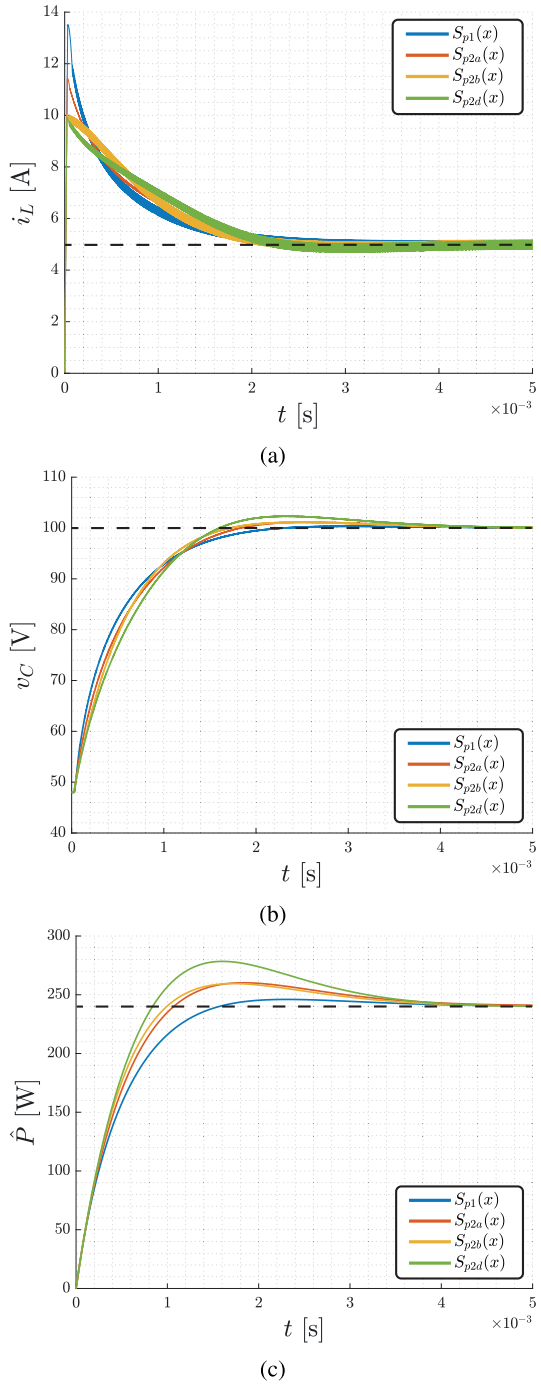

FIGURE 15. PSIM© simulation showing the state variables during start-up for polynomial surfaces with $R = 4$ Ω. (a) i_L. (b) v_C. (c) $\hat{P}$.

In order to reduce E_p to zero, the input voltage V_g could be substituted in the surfaces by a modified input voltage $\hat{V}_g$ that would include the power losses produced by R_{Loss} as follows

$$\hat{V}_g = \frac{V_g + \sqrt{V_g^2 - 4\hat{P}R_{Loss}}}{2}$$
$$\hat{V}_g < V_g \qquad (35)$$

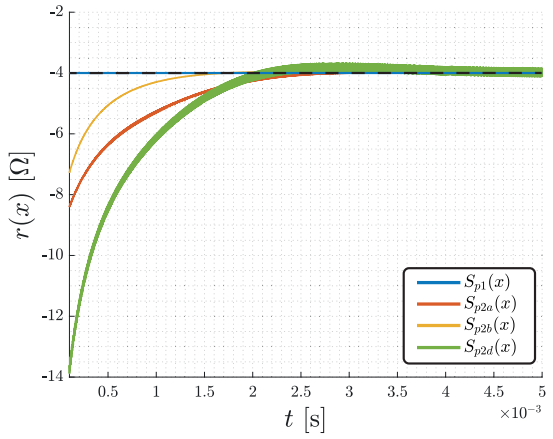

FIGURE 16. Incremental resistance $r(x)$ vs time along the trajectory from x_0 for $R = 4$ Ω.

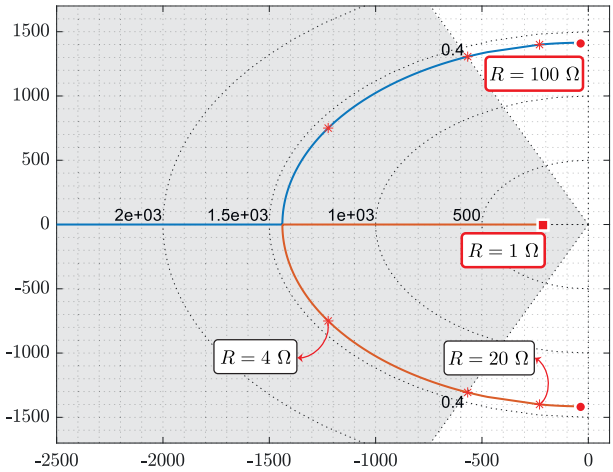

FIGURE 17. Location of the closed-loop poles for different values of the incremental resistance, $\beta = 10$ kA/s and $P = 240$ W.

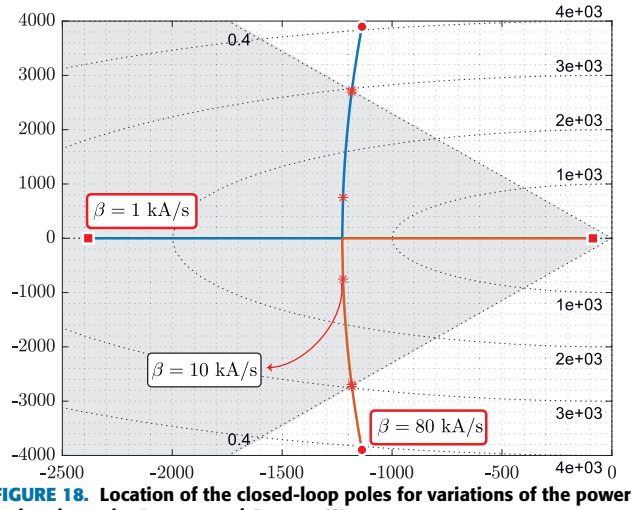

FIGURE 18. Location of the closed-loop poles for variations of the power estimation gain, $R = 4$ Ω and $P = 240$ W.

VI. EXPERIMENTAL RESULTS

A 500 W prototype has been built with an affine sliding surface for the converter parameters and reference values in Table 5. Fig. 20 shows the schematic circuit of the boost converter with a CPL emulated by an electronic load EA-EL 9160-300. The power semiconductors are a dual diode VX60M100PWHM3 for both D and D_r and a MOSFET STW56N60M2, which is activated by an isolated driver TLP350H. The currents i_L and i_o are measured by sensors LEM LA25 with gains of 1/10, while voltages V_g and v_C are measured with LEM LM-25 with gains of 1/100.

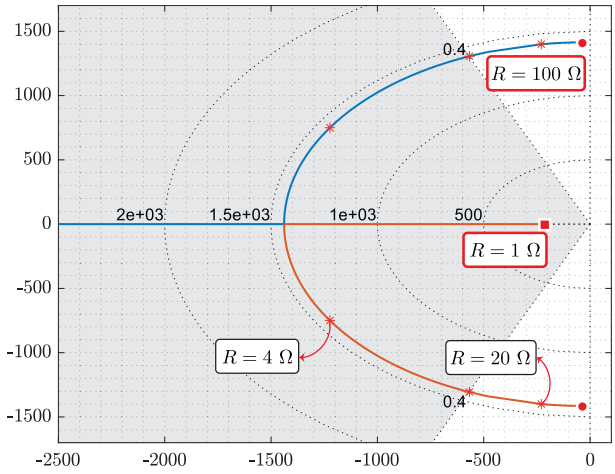

FIGURE 19. Location of the closed-loop poles for variations of output power, $R = 4$ Ω and $\beta = 10$ kA/s.

Fig. 21 illustrates the circuit scheme of the sliding-mode controller implemented by means of analog circuitry. The practical analog implementation of the control law requires a hysteresis comparator to establish a finite switching frequency. Fig. 21 shows the hysteresis modulator with a width of 2Δ made up of two comparators of the integrated circuit (IC) LM3198 and a J-K flip-flop CD4027, and whose input is the switching function $-S(x)$. The hysteresis band goes from $-\Delta$ to $+\Delta$, and these limits are set by means of a potentiometer, a follower and inverter stage based on the operational amplifier (OA) LF347. The hysteresis width has been adjusted to obtain a switching frequency constrained between 120 and 175 kHz.

The switching function $-S(x)$ for the affine function $S_{p1}(x) = a_1(i_L - \hat{P}/V_g) + b_1(v_C - V_e)$ is obtained in the circuit of Fig. 21b by adding an inverter. The coefficients of the switching function a_1 and b_1 are adjusted by two potentiometers, which modifies the gains of current error $e_i = i_L - \hat{P}/V_g$ and voltage error $e_v = v_C - V_e$, respectively. The reference current $\hat{P}/V_g$ is calculated by a divider implemented with the analog device AD633 and the OA LF347, while obtaining the estimated power $\hat{P}$ requires a single integrator processing the voltage error as shown in Fig. 21c, which is implemented with the same OA. In order to guarantee a zero initial value at the output of the integrator, a bilateral switch CD4016 is used to short-circuit the feedback path only before starting the power estimation.

Experimental setup involves a power generator AMETEK AMREL SPS800 × 13-K02D as input voltage source,

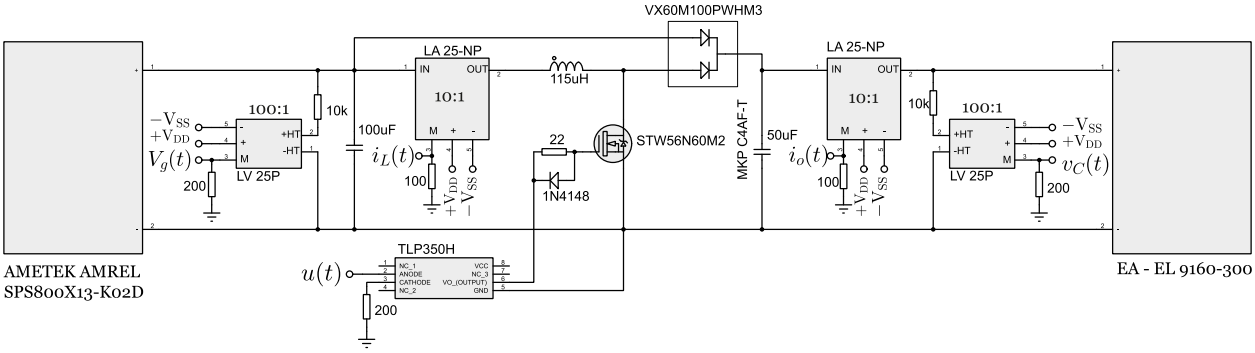

FIGURE 20. Circuit schematic of the power stage.

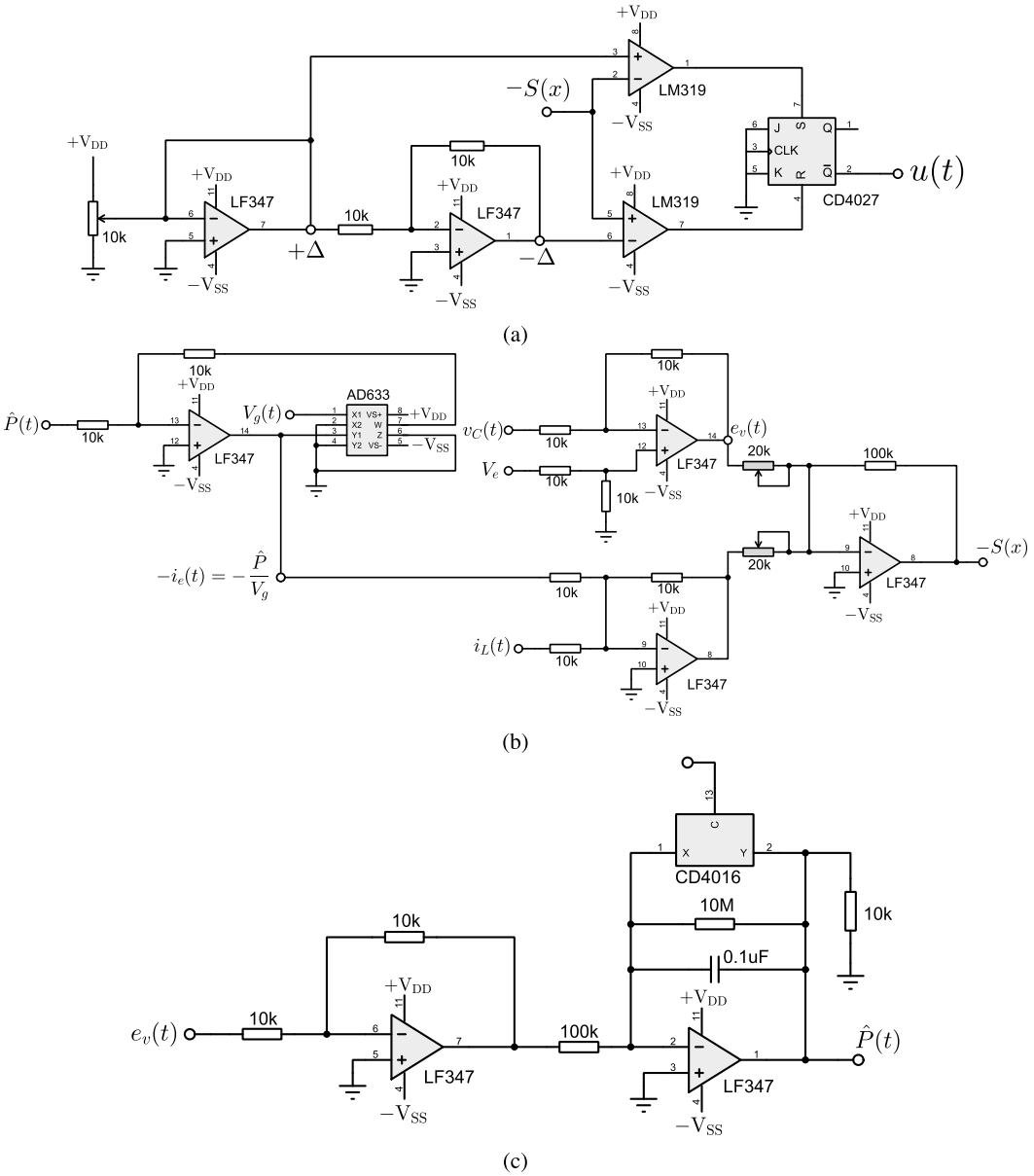

FIGURE 21. Circuit scheme of the sliding mode controller. (a) Hysteresis modulator. (b) Switching surface for affine function. (c) Linear power estimator.

A programmable load EA-EL9160-300 configured as a CPL, a oscilloscope Tektronix MDO 3014 with current probe TCP0020 and isolated voltage probe THDP0200. A picture of the complete experimental setup is shown in Fig. 22.

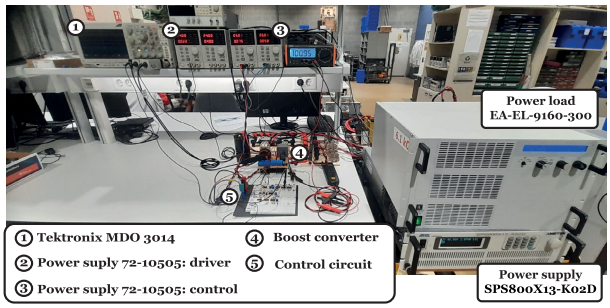

FIGURE 22. Picture of an overall view of the experimental setup.

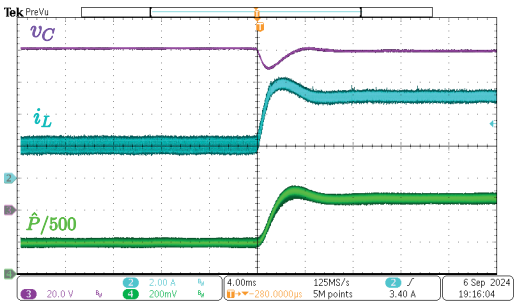

(a)

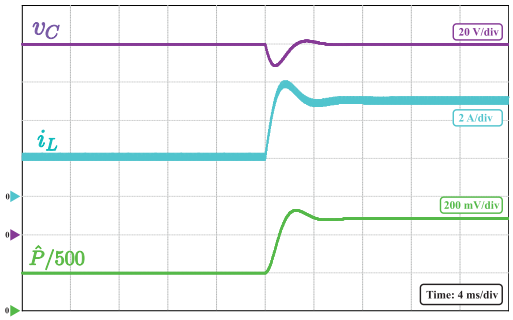

(b)

FIGURE 23. Transient response for an abrupt load power variation between 100 W to 240 W for $R = 6.71\ \Omega$. (a) Experimental. (b) PSIM© simulation.

A. DYNAMIC PERFORMANCE UNDER LOAD POWER VARIATION

In order to validate the proposed sliding mode control with power load estimation, a test has been performed to measure the system performance under load power variations. According to the theoretical analysis of Section V using the parametric values of Table 5, a suitable value for the incremental resistance R will be between 4 Ω and 20 Ω. Thus, the potentiometers related to the current and voltage error have been adjusted for $a_1 = 0.6341$ (100 kΩ/15.77 kΩ) and $b_1 = 0.945$ (100 kΩ/10.58 kΩ), corresponding to an incremental resistance $|r(x)|_{X_e} = -R = -6.71\ \Omega$. The value of the estimation loop gain β is -10 kA/s, which corresponds to an integration gain of 100. The magnitude of the estimated power signal in the control circuit has a reducing factor of $1/10^4$, requiring an additional amplifier stage with a gain of 20 to be observed.

Fig. 23 shows the comparison of experimental and simulation responses for a variation of the load power from 100 W to 240 W. The PSIM© simulation has taken into account the sensing and control stages depicted in Figs. 20 and 22, and the measured parasitic series resistance of the inductor with a value of 0.1 Ω in order to compare experimental and simulation on an equal basis. Both dynamic responses for a load disturbance of step type are in good agreement showing an output voltage recovery time of around 4 ms, convergence of the estimated power to the nominal value, and a maximum voltage deviation of 12 V approximately. These results are consistent with the theoretical response of the small-signal model, as it can be seen in Fig. 24, despite the large variation in load power of 2.4 times the initial value. This also explains the large output voltage deviation of 12% with respect to nominal value in the test. The settling time less than 4 ms

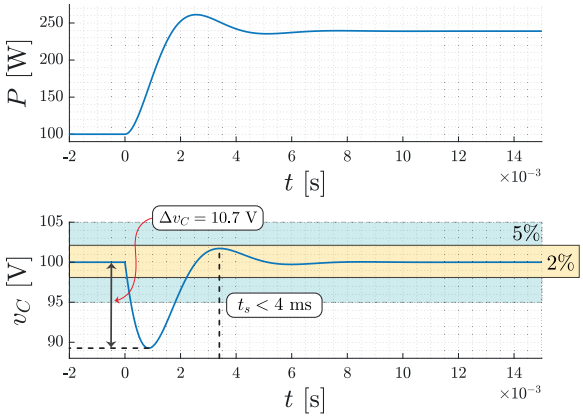

FIGURE 24. Small-signal model response for a power load variation between 100 W to 240 W for $R = 6.71\ \Omega$.

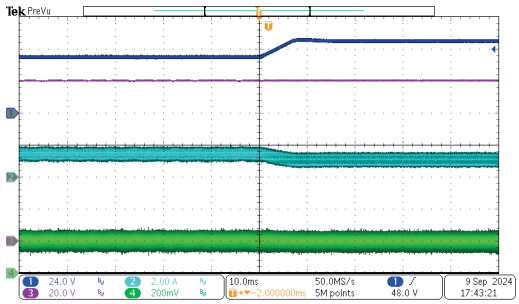

(a)

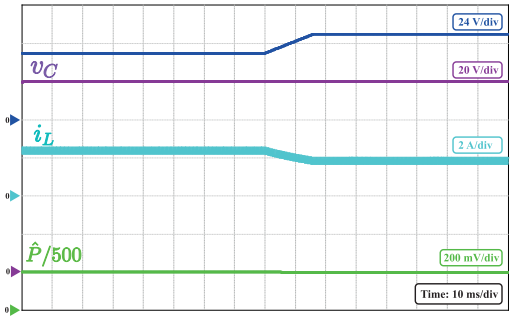

(b)

FIGURE 25. Transient response for input voltage variation from 42 V to 54 V with a power load of 100 W. (a) Experimental. (b) PSIM© simulation.

TABLE 7. Comparison of different proposals of control with load power estimation.

Reference	Control technique	Power calculation technique	Analytical framework	Complexity of control signal calculation	Implementation
[24]	Interconnection and damping assignment passivity-based controller (IDA-PBC)	Immersion & invariance technique (I&I technique)	Continuous-time analysis on an average model of the converter	High	N/A
[25]	Energy-based control	Disturbance observer	Continuous-time analysis on an average model of the converter	High	Digital. Sampling time of 2 kHz, fixed switching frequency of 100 kHz. TI MSP430F5132
[26]	Power shaping controller (PSC)	I&I technique	Continuous-time analysis on an average model of the converter	High	Digital. Sampling time of 2 kHz, fixed switching frequency of 100 kHz. Processing core ARM-Cortex-M0
[27]	Passivity based controller (PBC)	I&I technique	Continuous-time analysis on an average model of the converter	High	Digital. Fixed switching frequency of 100 kHz. Processing core ARM-Cortex-M0
[28]	PBC	generalized parameter estimation-based observer (GPEBO). Dynamic regressor extension and mixing (DREM) method	Continuous time analysis on an average model of the converter	High	Digital. Sampling time of 2 kHz, fixed switching frequency of 100 kHz. Processing core ARM-Cortex-M0
[29]	Model predictive control (MPC)	Higher order sliding mode observer (HOSMO)	Continuous-time analysis on the switched model	High	Digital. Fixed switching frequency of 20 kHz. dSPACE DS1006
[30]	Discretized quasi-sliding mode control (DQSMC)	second-order sliding mode disturbance	Discrete-time analysis	High	Digital. Fixed switching frequency of 20 kHz. dSPACE DS110
Proposal	Polynomial sliding mode control	Integrator over voltage error function	Continuous-time analysis on the switched model	Low	Analog. Variable switching frequency with average value of 150 kHz

corresponds to a band of 2% around the nominal output voltage. If 5% error margin were considered, the settling time value would be less than 2 ms.

B. DYNAMIC PERFORMANCE UNDER INPUT VOLTAGE VARIATION

The calculation of current reference $I_e = \hat{P}/V_g$ by means of analog circuitry and the direct measurement of input voltage V_g provides an adaptive way to setting the current reference, which is restricted by the bandwidth of the voltage sensor, multiplier AD633 and OA LF347. This configuration for the reference current results in the rejection of disturbances in the input voltage.

Fig. 25 illustrates the transient response to a variation in the input voltage between 42 V and 54 V (around $\pm 12\%$ from nominal input voltage) with a slope of 1.5 V/ms. The inductor current i_L changes following the gradual variation of the input voltage, but the output voltage and estimated power remain practically unaltered. Due to the conduction losses, there is a deviation of the real value of power load in the power estimation loop of around 0.9 W, which represents an error less than 1% of the nominal power load, but it is not appreciated in the figures.

VII. COMPARATIVE WITH OTHER PROPOSALS

The experimental evaluation of the sliding-mode controllers based on polynomial switching functions incorporating a power estimation loop exhibits good dynamic behavior in both output voltage regulation and CPL power calculation and requires few design parameters. To put the effectiveness of our proposal into context, we present in this section a comparative analysis with the previous works commented in the introduction.

Firstly, Table 7 shows the type of control and the method used for power estimation in previous works and in our proposal. The column with the control complexity label reflects (i) both type and number of mathematical operations required to calculate the control signal and power estimation value, and (ii) the number of parameters for the design. It can be observed that the complexity of our proposal is lower than the one corresponding to other control methods because it requires only three design parameters (a_1, b_1 and β), four arithmetic operations and an integrator to calculate the control signal and the estimated power load, which eventually results in the simplest implementation. It is worth mentioning that all the controllers and power estimators in the previous works were digitally implemented,

TABLE 8. Comparison of experimental dynamic response.

Reference	Converter	Maximum power	Time response for step power load variation
[24]	Buck-boost	30 W	40 ms. 1.6% deviation from rated voltage with 50% change in rated power
[25]	Buck	18 W	20 ms. 6.2% deviation from rated voltage with 50% change in rated power
[26]	Buck	25 W	N/A
[27]	Buck	35 W	200 ms. 8.34% deviation from rated voltage with 400% change in rated power
[28]	Interleaved buck	36 W	N/A
[29]	Buck	1500 W	2 ms. 3% deviation from rated voltage with 200% change in rated power
[30]	Buck	400 W	$<$ 2 ms. 5% deviation from rated voltage with 100% change in rated power
Proposal	Boost	240 W	$<$ 4 ms. 10.7% deviation from rated voltage with 140% change in rated power

which creates a heterogeneous basis for comparison with respect to the analogical proposal presented in this paper. Another important point is that, with the exception of [30], all the previous methods are analyzed in continuous-time omitting the necessary discretization analysis before the digital implementation and skipping its implications in the controller and power estimator performance.

Secondly, Table 8 shows the settling time and the output voltage deviation relative to the nominal value in response to a variation in the CPL power. The data of some previous works were approximately calculated from image observation of the experimental results reported in each paper, due to the absence of an explicit mention of such values in the text. In case of complete absence of images or impossibility to determine a value due to low image resolution, the acronym N/A is used. It can be observed that the work here reported, i.e. SMC with polynomial switching surfaces, presents excellent performance in both settling time and output voltage deviation outperforming most of the previous methods.

The best performance was obtained for the buck converter in both [29], [30] where both the controller and estimator are based on a SMC approach. However, the buck converter is a minimum phase system in contrast to the boost converter considered in this study which is a in a non-minimum phase system. Therefore, one of the reason for the excellent performance in [29] and [30] should be attributed partially to the power stage used and not exclusively to the controller and the estimator.

VIII. CONCLUSION

The use of an integral loop of output voltage error within a sliding mode controller using polynomial surfaces has demonstrated the feasible and efficient estimation of the power load in a boost converter with CPL guaranteeing voltage regulation with zero steady-state error. The result is a sliding mode control–based switching regulator with adaptive characteristics.

From a general two-degree polynomial switching surface in the phase plane $i_L - v_C$, the inclusion of the power estimation loop based on the integral of a function of the output voltage error satisfies both the condition for the existence of sliding motions and the stability criterion for an appropriate selection of the surface coefficients.

The general switching surface has been particularized in five canonical curves, i.e. one linear curve and four conic curves; namely, an affine function, a current parabola, a voltage parabola, a cross-power hyperbola, and an ellipse. All these surfaces use constant coefficients, this keeping the curve shape during transients in a cleat-cut contrast with other proposed surfaces in the literature.

In addition, a general description of the voltage error function $f(e_v)$ has been defined and the necessary conditions that the function must fulfill have been established. The latter are odd symmetric and negative slope at $e_v = 0$, the linear expression $-\beta e_v$ being the simplest one. Different candidates for the voltage error function have been classified in four categories: rational functions, trigonometric functions, sigmoid functions, and first-order sliding estimators by means of sign function with hysteresis. Operating conditions have been determined for each type of function together with well-defined estimation limits.

The small-signal dynamics of the controller with power estimation in sliding motion has been defined in terms of the incremental resistance $|r(x)|_{X_e} = -R$ and the power estimation gain β irrespective of the type of polynomial surface. The small-signal analysis has allowed establishing a recommended range of operation considering the maximum power load P_{max} and the power estimation gain β_{max}. The conclusions of the analysis can be extrapolated for a qualitative description of the large-signal operation after

studying the closed-loop control for start-up from initial conditions up to a desired EP. It can be concluded that a high value of the power estimation gain allows reaching the sliding surface in a shorter time during start-up. Also, it has been demonstrated that the incremental resistance R plays a central role in determining the dynamic performance of the system since a correct selection of R guarantees similar dynamic characteristics in the whole operating range of the converter.

A final global assessment that considers both dynamic performance and implementation complexity allows to summarize that: (i) the affine surface is the best candidate among the polynomial surfaces because it keeps the incremental resistance constant along the state vector trajectory from initial conditions to EP, and its implementation requires a minimum number of circuit elements; and (ii) the linear estimator is the simplest theoretical solution to be inserted in an analog sliding mode controller.

Numerical analysis based on MATLAB© and PSIM© simulations, and experimental results have verified the theoretical predictions. The dynamic performance has been evaluated for large-signal variations of output load power and input voltage.

The preliminary analysis of first-order sliding-mode estimator has shown their feasibility and exposed the problem of the associated chattering. An extension to higher-order sliding estimators to minimize the chattering is contemplated in our further research.

REFERENCES

[1] S. C. Smithson and S. S. Williamson, "Constant power loads in more electric Vehicles–an overview," in *Proc. IECON 38th Annu. Conf. IEEE Ind. Electron. Soc.*, Oct. 2012, pp. 2914–2922.

[2] P. Lindman and L. Thorsell, "Applying distributed power modules in telecom systems," in *Proc. IEEE Appl. Power Electron. Conf. Expo. (ASPEC)*, Mar. 1994, pp. 777–785.

[3] A. Kwasinski and C. N. Onwuchekwa, "Dynamic behavior and stabilization of DC microgrids with instantaneous constant-power loads," *IEEE Trans. Power Electron.*, vol. 26, no. 3, pp. 822–834, Mar. 2011.

[4] A. M. Rahimi and A. Emadi, "Discontinuous-conduction mode DC/DC converters feeding constant-power loads," *IEEE Trans. Ind. Electron.*, vol. 57, no. 4, pp. 1318–1329, Apr. 2010.

[5] B. Choi, B. H. Cho, and S.-S. Hong, "Dynamics and control of DC-to-DC converters driving other converters downstream," *IEEE Trans. Circuits Syst. I, Fundam. Theory Appl.*, vol. 46, no. 10, pp. 1240–1248, Oct. 1999.

[6] M. Cespedes, L. Xing, and J. Sun, "Constant-power load system stabilization by passive damping," *IEEE Trans. Power Electron.*, vol. 26, no. 7, pp. 1832–1836, Jul. 2011.

[7] G. Sulligoi, D. Bosich, G. Giadrossi, L. Zhu, M. Cupelli, and A. Monti, "Multiconverter medium voltage DC power systems on ships: Constant-power loads instability solution using linearization via state feedback control," *IEEE Trans. Smart Grid*, vol. 5, no. 5, pp. 2543–2552, Sep. 2014.

[8] A. M. Rahimi and A. Emadi, "Active damping in DC/DC power electronic converters: A novel method to overcome the problems of constant power loads," *IEEE Trans. Ind. Electron.*, vol. 56, no. 5, pp. 1428–1439, May 2009.

[9] Y. Li, K. R. Vannorsdel, A. J. Zirger, M. Norris, and D. Maksimovic, "Current mode control for boost converters with constant power loads," *IEEE Trans. Circuits Syst. I, Reg. Papers*, vol. 59, no. 1, pp. 198–206, Jan. 2012.

[10] M. Sebastià-Rullo, A. Cid-Pastor, H. Valderrama-Blavi, A. E. Aroudi, and L. Martínez-Salamero, "Series loss-free resistor as stabilizing active damping of constant-power load systems," *IEEE Trans. Circuits Syst. I, Reg. Papers*, vol. 71, no. 12, pp. 5847–5860, Dec. 2024.

[11] C. N. Onwuchekwa and A. Kwasinski, "Analysis of boundary control for buck converters with instantaneous constant-power loads," *IEEE Trans. Power Electron.*, vol. 25, no. 8, pp. 2018–2032, Aug. 2010.

[12] V. Utkin, J. Guldner, and J. Shi, *Sliding Mode Control in Electro-Mechanical Systems*, 2nd ed., Boca Raton, FL, USA: CRC Press, 2017.

[13] L. Benadero, R. Cristiano, D. J. Pagano, and E. Ponce, "Nonlinear analysis of interconnected power converters: A case study," *IEEE J. Emerg. Sel. Topics Circuits Syst.*, vol. 5, no. 3, pp. 326–335, Sep. 2015.

[14] S. Singh, D. Fulwani, and V. Kumar, "Robust sliding-mode control of DC/DC boost converter feeding a constant power load," *IET Power Electron.*, vol. 8, no. 7, pp. 1230–1237, Jul. 2015.

[15] S. Singh and D. Fulwani, "Constant power loads: A solution using sliding mode control," in *Proc. IECON 40th Annu. Conf. IEEE Ind. Electron. Soc.*, Oct. 2014, pp. 1989–1995.

[16] S. Singh, V. Kumar, and D. Fulwani, "Mitigation of destabilising effect of CPLs in island DC micro-grid using non-linear control," *IET Power Electron.*, vol. 10, no. 3, pp. 387–397, Mar. 2017.

[17] N. Tiwary, N. V. R. Naik, A. K. Panda, R. K. Lenka, and A. Narendra, "Sliding mode and current observer-based direct power control of dual active bridge converter with constant power load," *Int. Trans. Electr. Energy Syst.*, vol. 31, no. 5, Mar. 2021, Art. no. e12879.

[18] B. A. Martinez-Treviño, A. El Aroudi, E. Vidal-Idiarte, A. Cid-Pastor, and L. Martinez-Salamero, "Sliding-mode control of a boost converter under constant power loading conditions," *IET Power Electron.*, vol. 12, no. 3, pp. 521–529, Mar. 2019.

[19] D. A. Zambrano-Prada, A. El Aroudi, L. Vázquez-Seisdedos, and L. Martínez-Salamero, "Polynomial sliding surfaces to control a boost converter with constant power load," *IEEE Trans. Circuits Syst. I, Reg. Papers*, vol. 70, no. 1, pp. 530–543, Jan. 2023.

[20] C. A. Torres-Pinzón, F. Flores-Bahamonde, J. A. Garriga-Castillo, H. Valderrama-Blavi, R. Haroun, and L. Martínez-Salamero, "Sliding-mode control of a quadratic buck converter with constant power load," *IEEE Access*, vol. 10, pp. 71837–71852, 2022.

[21] M. Boukerdja, A. Chouder, L. Hassaine, B. O. Bouamama, W. Issa, and K. Louassaa, "H∞ based control of a DC/DC buck converter feeding a constant power load in uncertain DC microgrid system," *ISA Trans.*, vol. 105, pp. 278–295, Oct. 2020.

[22] W. He, Y. Zhang, and W. Zhou, "Observerless output feedback control of DC–DC converters feeding a class of unknown nonlinear loads via power shaping," *IEEE Trans. Circuits Syst. I, Reg. Papers*, vol. 71, no. 6, pp. 2951–2963, Jun. 2024.

[23] W. He, R. Ortega, J. E. Machado, and S. Li, "An adaptive passivity-based controller of a buck-boost converter with a constant power load," *Asian J. Control*, vol. 21, no. 1, pp. 581–595, Jan. 2019.

[24] W. He, C. A. Soriano-Rangel, R. Ortega, A. Astolfi, F. Mancilla-David, and S. Li, "Energy shaping control for buck–boost converters with unknown constant power load," *Control Eng. Pract.*, vol. 74, pp. 33–43, May 2018.

[25] W. He, M. M. Namazi, and J. M. Guerrero, "Adaptive energy-based control for buck converter with a class of nonlinear loads," *IEEE Trans. Circuits Syst. II, Exp. Briefs*, vol. 69, no. 12, pp. 4869–4873, Dec. 2022.

[26] W. He, M. M. Namazi, H. R. Koofigar, M. A. Amirian, and J. M. Guerrero, "Voltage regulation of buck converter with constant power load: An adaptive power shaping control," *Control Eng. Pract.*, vol. 115, Oct. 2021, Art. no. 104891.

[27] W. He, M. M. Namazi, H. R. Koofigar, M. A. Amirian, and F. Blaabjerg, "Stabilization of DC–DC buck converter with unknown constant power load via passivity-based control plus proportion-integration," *IET Power Electron.*, vol. 14, pp. 2597–2609, Dec. 2021.

[28] W. He, Y. Shang, M. M. Namazi, and R. Ortega, "Adaptive sensorless control for buck converter with constant power load," *Control Eng. Pract.*, vol. 126, Sep. 2022, Art. no. 105237.

[29] Q. Xu, Y. Yan, C. Zhang, T. Dragicevic, and F. Blaabjerg, "An offset-free composite model predictive control strategy for DC/DC buck converter feeding constant power loads," *IEEE Trans. Power Electron.*, vol. 35, no. 5, pp. 5331–5342, May 2020.

[30] C. Zheng, T. Dragicevic, J. Zhang, R. Chen, and F. Blaabjerg, "Composite robust quasi-sliding mode control of DC–DC buck converter with constant power loads," *IEEE J. Emerg. Sel. Topics Power Electron.*, vol. 9, no. 2, pp. 1455–1464, Apr. 2021.

[31] W. He and R. Ortega, "Design and implementation of adaptive energy shaping control for DC–DC converters with constant power loads," *IEEE Trans. Ind. Informat.*, vol. 16, no. 8, pp. 5053–5064, Aug. 2020.

[32] M. A. Hassan, C.-L. Su, F.-Z. Chen, and K.-Y. Lo, "Adaptive passivity-based control of a DC–DC boost power converter supplying constant power and constant voltage loads," *IEEE Trans. Ind. Electron.*, vol. 69, no. 6, pp. 6204–6214, Jun. 2022.
[33] Q. Xu, C. Zhang, C. Wen, and P. Wang, "A novel composite nonlinear controller for stabilization of constant power load in DC microgrid," *IEEE Trans. Smart Grid*, vol. 10, no. 1, pp. 752–761, Jan. 2019.
[34] N. Rathore, D. Fulwani, A. K. Rathore, and A. R. Gautam, "Adaptive sliding mode based loss-free resistor for power-factor correction application," *IEEE Trans. Ind. Appl.*, vol. 55, no. 4, pp. 4332–4343, Jul. 2019.
[35] G. E. Mejia-Ruiz, M. R. A. Paternina, J. A. de la O Serna, and A. Zamora-Mendez, "O splines-based fixed-frequency integral sliding-mode controller for PFC rectifier," *IEEE Trans. Power Electron.*, vol. 38, no. 8, pp. 9448–9458, Aug. 2023.
[36] B. A. Martínez-Treviño, A. E. Aroudi, H. Valderrama-Blavi, A. Cid-Pastor, E. Vidal-Idiarte, and L. Martinez-Salamero, "PWM nonlinear control with load power estimation for output voltage regulation of a boost converter with constant power load," *IEEE Trans. Power Electron.*, vol. 36, no. 2, pp. 2143–2153, Feb. 2021.
[37] D. Zambrano-Prada, A. E. Aroudi, L. Vázquez-Seiszdedos, O. Lopez-Santos, R. Haroun, and L. Martínez-Salamero, "Adaptive sliding mode control for a boost converter with constant power load," in *Proc. IEEE Conf. Power Electron. Renew. Energy (CPERE)*, Feb. 2023, pp. 1–6.
[38] S. Singer and R. W. Erickson, "Canonical modeling of power processing circuits based on the POPI concept," *IEEE Trans. Power Electron.*, vol. 7, no. 1, pp. 37–43, Jan. 1992.

DAVID A. ZAMBRANO-PRADA received the electronic engineer and master's degrees in control engineering from the Universidad de Ibagué, Colombia, in 2014 and 2019, respectively, and the Ph.D. degree from Universitat Rovira i Virgili, Spain, in 2023. From 2015 to 2019, he was a Young Researcher with the D+TEC Research Group, Universidad de Ibagué, in control of dc–dc converters, energy storage systems, and microgrids. In 2020, he joined the Automatic Control and Industrial Electronics Research Group (GAEI), Universitat Rovira i Virgili, where he is currently a Postdoctoral Researcher. His research interests include control of energy storage systems within dc microgrids, electric vehicles, dc–dc converters, and sliding mode control.

ABDELALI EL AROUDI (Senior Member, IEEE) received the bachelor's degree in physical science from the Faculté des Sciences, Université Abdelmalek Essaadi, Tetouan, Morocco, in 1995, and the Ph.D. degree (Hons.) in applied physical science from the Universitat Politècnica de Catalunya, Barcelona, Spain, in 2000. He is currently a Full Professor with the Department of Electronics, Electrical Engineering and Automatic Control, Universitat Rovira i Virgili, Tarragona, Spain. His research interests include dynamics and control of power conditioning systems, power factor correction, and renewable energy applications. He was an Associate Editor of the *IET Circuits, Devices and Systems*, the *IET Power Electronics*, and the *Electronics Letters* (IET). He was the Guest Editor of the IEEE JOURNAL ON EMERGING AND SELECTED TOPICS IN CIRCUITS AND SYSTEMS, in 2015, IEEE TRANSACTIONS ON CIRCUITS AND SYSTEMS—II: EXPRESS BRIEFS, in 2018, and *Energies*, from 2018 to 2023. He also serves as an Associate Editor for *International Journal of Circuit Theory and Applications* and the Topic Editor for *Energies*.

OSWALDO LÓPEZ-SANTOS (Senior Member, IEEE) received the Electronic Engineering degree from the Universidad Distrital Francisco José de Caldas, Bogotá, Colombia, in 2002, the master's degree in industrial automation from the Universidad Nacional de Colombia, Bogotá, in 2011, and the Ph.D. degree from the Institut National des Sciences Appliquées (INSA) de Toulouse, in 2015. From 2004 to 2008, he was in Colombia, as a Design Engineer, for manufacture of industrial power converters. From 2009 to 2021, he was an Associate Professor with the Electronics Engineering Department and the Leader of the Research Group Technological Development (D+TEC), Universidad de Ibagué, Colombia. In 2020, he was with D+Tec, Universidad de Ibaguá, as the Director of the Research Office. He is currently a Postdoctoral Research Associate with the Research Group GAEI, Universitat Rovira i Virgili, Tarragona, Spain. He is Developing his research project at LAAS-CNRS. His current research interests include the control of power electronic converters involved in applications, such as microgrids and electric vehicles.

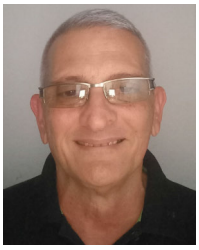

LUIS VÁZQUEZ-SEISDEDOS received the B.S. degree in automatic control engineering, the M.S. degree in automation, and the Ph.D. degree in technical science (automation) from the Universidad de Oriente, Santiago de Cuba, Cuba, in 1982, 1999, and 2015, respectively, and the Ph.D. degree in nanosystems technologies, bioengineering and energy from Rovira i Virgili University, Spain, in 2022. His research interests include the control of electromechanical energy conversion systems, namely, power plants based on both fossil fuel sources and renewable energy resources (RES), electric vehicles (EV), energy storage subsystems and its hybridization, electric drives, electrical traction systems, and RES's and EV's integration into electrical power systems. Since 2009, he has been a member of the TC 6.3. Power and Energy Systems Committee of IFAC.

LUIS MARTÍ-NEZ-SALAMERO (Life Senior Member, IEEE) received the Ingeniero de Telecomunicacion and Ph.D. degrees from the Universidad Politecnica de Cataluna, Barcelona, Spain, in 1978 and 1984, respectively, and the Doctor Honoris Causa degree from Université Toulouse III Paul Sabatier, France, in 2024. From 1978 to 1992, he taught circuit theory, analog electronics, and power processing at the Escuela Técnica Superior de Ingenieros de Telecomunicación, Barcelona, Spain. From 1992 to 1993, he was a Visiting Professor with the Center for Solid State Power Conditioning and Control, Department of Electrical Engineering, Duke University, Durham, NC, USA. From 2003 to 2004, 2010 to 2011, and March to September 2018, he was a Visiting Scholar with the Laboratory of Architecture and Systems Analysis (LAAS), National Agency for Scientific Research (CNRS), Toulouse, France. Since 1995, he has been a Full Professor with the Department of Electrical Electronic and Automatic Control Engineering, School of Electrical and Computer Engineering, Rovira i Virgili University, Tarragona, Spain, where he managed the Research Group in Automatic Control and Industrial Electronics (GAEI), from 1998 to 2018. His research interests include structure and control of power conditioning systems, namely, electrical architecture of satellites and electric vehicles, as well as nonlinear control of converters and drives, and power conditioning for renewable energy.